Three-dimensional turbulent Navier-Stokes hydrodynamic analysis and performance assessment of oscillating wings for power generation

Jernej DROFELNIK[1], M.Sergio CAMPOBASSO[2],

[1] University of Glasgow, School of Engineering. James Watt Building South, University Avenue, Glasgow G12 8QQ, United Kingdom. E-mail: j.drofelnik.1@research.gla.ac.uk
[2] Corresponding Author. University of Lancaster, Department of Engineering. Engineering Building, Gillow Avenue, Lancaster LA1 4YW, United Kingdom. Tel.: +44 (0)1524 594673, E-mail: m.s.campobasso@lancaster.ac.uk

ABSTRACT

A wing simultaneously heaving and pitching can extract energy from an oncoming water or air stream. First large-scale commercial demonstrators are being installed and tested. The operating conditions of this device is likely to feature Reynolds numbers in excess of 500,000. Strong finite wing effects spoiling the power generation efficiency are also expected. This paper thoroughly investigates the hydrodynamics of oscillating wings at a Reynolds number of 1,500,000 considering finite wing effects for an aspect ratio 10 wing with either sharp tips or endplates to reduce tip vortex losses. The study of these periodic flows uses three-dimensional time-dependent Navier-Stokes simulations with grids featuring more than 30 million cells The shear stress turbulence model of Menter is used for the turbulence closure. Main contributions include: *a*) the quantification of the efficiency improvement achievable by using wings with endplates rather than bare tips, and *b*) detailed comparisons of the wing hydrodynamics with and without endplates, and the infinite wing,

Keywords: Energy-extracting oscillating wing, Finite wing effects, Turbulent Navier-Stokes CFD

1. INTRODUCTION

Increasing demand for electricity production and stricter environmental policy have greatly contributed to the development of novel alternative renewable devices. A promising concept in the fields of wind turbines and tidal energy systems relies on the use of oscillating wings simultaneously heaving and pitching to extract energy from an oncoming water or air stream. The concept was pioneered by McKinney and DeLaurier [1] in 1981, and further investigated by Jones *et al.* [2]. Several other numerical, experimental and prototype-based studies of the oscillating wing device for power generation followed these pioneering studies. Recently Young *et al.* [3] published a comprehensive review of the analytical, numerical and experimental research work carried out in this field to date. The review focuses on the effects of flapping kinematics and foil geometry on the vortex-structure interaction, a phenomenon that can improve the power generation efficiency for certain laminar and turbulent flow regimes. That article also highlights outstanding questions on the fluid mechanics of the oscillating wing in real installations, characterized by high Reynolds numbers and strong and complex three-dimensional (3D) flow effects. available literature.

Kinsey and Dumas [4] performed a thorough parametric computational fluid dynamics (CFD) investigation into the effects of motion parameters (heaving and pitching amplitude and motion frequency) and geometric parameters (foil shape and location of pitching axis) on the power generation efficiency of the oscillating wing. They report that using optimum motion parameters for a laminar flow regime with a Reynolds number based on the foil chord and the freestream velocity of 1100 yields an efficiency of 34%, and also that the main factor controlling the efficiency is the synchronization of heaving motion and unsteady leading edge vortex shedding (LEVS) associated with dynamic stall. These findings were confirmed also in a later study using the compressible Navier-Stokes (NS) research code COSA with a low-speed preconditioner optimized for time-dependent flows [5].

An experimental 2 kW prototype of the oscillating wing for power generation was designed, built and tested by Laval university in water at Lac-Beauport near Quebec City. Measured data confirmed fairly high values of the energy conversion efficiency [6]. Thereafter Kinsey and Dumas investigated numerically the hydrodynamics of the oscillating wing at a Reynolds number of 0.5 mil-

lion [7]. Both two-dimensional (2D) and 3D turbulent incompressible FLUENT simulations using the Spalart-Allmaras turbulence model [8] were performed. Cross-comparison of the laminar and turbulent flow simulations using the same wing motion parameters reveals that the efficiency of the energy conversion increases significantly as the Reynolds number increases from low laminar values to fairly high turbulent values [4, 7, 9]. This was reported by the authors of this paper who used COSA to carry out 2D fully laminar [5] and fully turbulent [9] simulations of the oscillating wing using the same wing motion parameters. The comparative analysis of the two regimes reported in [9] revealed that a) the power generation efficiency increases at higher Reynolds numbers due to thinner turbulent boundary layers, b) LEVS is delayed in the fully turbulent regime due to higher stability of the turbulent bounary layers. Thus the optimal synchronization between wing motion and LEVS achieved in the laminar regime is lost in the high-Reynolds number case. It was assumed that for higher Reynolds numbers further synchronization of wing motion and LEVS could lead to even higher efficiencies than that of 40% obtained for turbulent regime.However, Kinsey and Dumas later showed that high power extraction efficiency at high Reynolds numbers does not necessarily rely on the occurrence of LEVS [10].

Kinsey and Dumas also reported that the power generation loss of the finite wing of aspect ratio (AR) 7 with endplates is about 15% of the efficiency of the infinite wing [7]. In a follow-up study, those authors extended their 3D analyses to wings of AR 5, 7 and 10 with and without endplates to quantify losses due to finite wing effects and wing tip type. They concluded that, for a finite wing of AR ≥ 10 with endplates such a loss could be limited to about 10% of the efficiency of infinite span [11].

The interest of the industrial and scientific communities in the oscillating wing device keeps growing, as also highlighted by the installation of the 1.2 MW prototype of Pulse Tidal in the Bristol Channel in 2014 [3]. However, significant uncertainty on the impact of 3D flow effects still exists. This study aims at quantifying the loss of power generation efficiency due to 3D effects making use of time-dependent (TD) finite wing span turbulent flow COSA simulations. Realistic turbulent flow conditions at a Reynolds number of 1.5 million and with nearly optimal wing motion parameters obtained with 2D analyses [9] are used, and the 3D effects are analysed for two different wing end geometries.

The paper sarts with the definition of the kinematic and dynamic parameters of the oscillating wing motion. This is followed by the statement of the governing equations and a brief description og the CFD solver. A detailed comparative study of the infinite and finite span wings in turbulent flow conditions is then reported, quantifying and discussing the differences of unsteady hydrodynamic characteristics

of the idealised 2D and realistic 3D configurations. A summary of the main findings are provided in the closing section.

2. OSCILLATING WING DEVICE
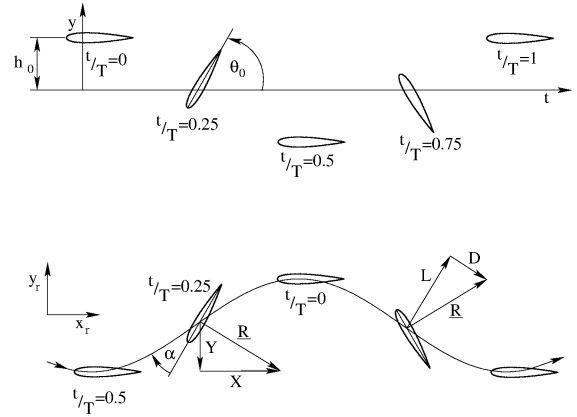
Figure 1. Top: prescribed motion of oscillating wing for power generation. Bottom: foil motion in reference system moving with freestream velocity.

Here an oscillating wing is defined as a foil experiencing simultaneous pitching $\theta(t)$ and heaving $h(t)$ motions. The following mathematical representation of the imposed motion is that adopted in [4]. Taking a pitching axis located on the chord line at position x_p from the leading edge (LE), the foil motion is expressed as:

$$\theta(t) = \theta_0 \sin(\omega t) \quad \rightarrow \Omega(t) = \theta_0 \omega \cos(\omega t) \quad (1)$$

$$h(t) = h_0 \sin(\omega t + \phi) \rightarrow v_y(t) = h_0 \omega \cos(\omega t + \phi) \quad (2)$$

where θ_0 and h_0 are respectively the pitching and heaving amplitudes, Ω is the pitching velocity, v_y is the heaving velocity, ω is the angular frequency and ϕ is the phase between heaving and pitching. In this study, ϕ is set to 90°, and the NACA0015 foil is selected. The freestream velocity is denoted by u_∞ and the angular frequency ω is linked to the vibration frequency f by the relationship $\omega = 2\pi f$. The prescribed oscillating motion is depicted in the top sketch of Fig. 1.

An oscillating symmetric foil can operate in two different regimes: propulsive or power-extracting mode. This distinction originates from the sign of the forces that the flow generates on the oscillating foil. Based on the imposed motion and the upstream flow conditions, the foil experiences an effective angle of attack (AoA) α and an effective velocity v_e given respectively by:

$$\alpha(t) = \arctan\left(-v_y(t)/u_\infty\right) - \theta(t) \quad (3)$$

$$v_e(t) = \sqrt{u_\infty^2 + v_y(t)^2} \quad (4)$$

The maximum values of α and v_e have a major impact on the amplitude of the peak forces in the cycle, and also on the occurrence of dynamic stall.

The maximum effective AoA reached in the cycle is approximated by the modulus of its quarter-period value, that is $\alpha_{max} \approx |\alpha(T/4)|$. As explained in [4], the power-extracting regime (in a mean sense, over one cycle) occurs when $\alpha(T/4) < 0$. This condition is represented in the bottom sketch of Fig. 1, which provides a time-sequence viewed in a reference frame moving with the farfield flow at u_∞, so that the effective AoA $\alpha(t)$ is made visible from the apparent trajectory of the foil. In this sketch, the resultant force $\underline{R}$ is first constructed from typical lift and drag forces (right-hand side) and then decomposed into X and Y components (left-hand side). One sees that the vertical force component Y is in phase with the vertical velocity component v_y of the foil over the entire cycle. This implies that the wing extracts energy from the fluid as long as no energy transfer associated with the component X of the hydrodynamic force takes place. This is the case since the foil does not move horizontally. The aerodynamic phenomena occurring during the wing oscillation are substantially more complex than the quasi-steady model discussed above. In some cases, for example, the efficiency of the energy extraction was shown to be heavily influenced by the occurrence of unsteady leading edge vortex shedding (LEVS) associated with dynamic stall and the LEVS timing with respect to the foil motion.

Taking a wing span of one unit length, the instantaneous power extracted from the flow is the sum of a heaving contribution $P_y(t) = Y(t)v_y(t)$ and a pitching contribution $P_\theta(t) = M(t)\Omega(t)$, where M is the resulting torque about the pitching center x_p. Denoting by c the foil chord, $C_{P_z} \equiv P_z/(\frac{1}{2}\rho_\infty u_\infty^3 c)$ the power coefficient per wing length at position z, and $C_P = \frac{1}{l}\int_{-l}^{l} C_{P_z}dz$ the power coefficient over the entire wing, where l denotes the semispan, the nondimensional power extracted over one cycle is given by:

$$\overline{C}_P = \overline{C}_{P_y} + \overline{C}_{P_\theta} = \frac{1}{T}\int_0^T \left[C_Y(t)\frac{v_y(t)}{u_\infty} + C_M(t)\frac{\Omega(t)c}{u_\infty} \right] dt$$

where $C_Y(t) = Y(t)/(\frac{1}{2}\rho_\infty u_\infty^2 c)$ and $C_M(t) = M(t)/(\frac{1}{2}\rho_\infty u_\infty^2 c^2)$.

3. NAVIER-STOKES CFD SOLVER

The finite volume structured multi-block compressible Reynolds-averaged NS (RANS) code COSA [5, 9, 12] uses Menter's shear stress transport (SST) turbulence model [13]. Given a moving control volume C with time-dependent boundary $S(t)$, the Arbitrary Lagrangian-Eulerian integral form of the system of the time-dependent RANS and SST equations is:

$$\frac{\partial}{\partial t}\left(\int_{C(t)} \mathbf{U}\, dC\right) + \oint_{S(t)} (\underline{\Phi}_c - \underline{\Phi}_d)\cdot d\underline{S} - \int_{C(t)} \mathbf{S}\, dC = 0$$

The array $\mathbf{U}$ of conservative flow variables is defined as: $\mathbf{U} = [\rho \quad \rho\underline{v}^T \quad \rho E \quad \rho k \quad \rho\omega]^T$ where ρ and $\underline{v}$ are respectively the fluid density and velocity vec-

tor, and E, k and ω are respectively the total energy, the turbulent kinetic energy and the specific dissipation rate of turbulent kinetic energy, all per unit mass. The perfect gas equation is used to link internal energy, pressure and density. The generalized convective flux vector $\underline{\Phi}_c$ depends on $\mathbf{U}$ and the velocity of the boundary S. The generalized diffusive flux vector $\underline{\Phi}_d$ depends primarily on the sum of the molecular stress tensor, proportional to the strain rate tensor $\underline{\underline{s}}$, and the turbulent Reynolds stress tensor. Adopting Boussinesq's approximation, the latter tensor is also proportional to $\underline{\underline{s}}$ through an eddy viscosity μ_T. In the SST model, μ_T depends on ρ, k, ω and the vorticity.

The only nonzero entries of the source term $\mathbf{S}$ are those of the k and ω equations, given respectively by:

$$S_k = \mu_T P_d - \frac{2}{3}(\nabla \cdot \underline{v})\rho k - \beta^* \rho k\omega$$

$$S_\omega = \gamma\rho P_d - \frac{2}{3}(\nabla \cdot \underline{v})\frac{\gamma\rho k}{\nu_T} - \beta\rho\omega^2 + CD_\omega$$

with

$$P_d = 2\left[\underline{\underline{s}} - \frac{1}{3}\nabla \cdot \underline{v}\right]\nabla\underline{v}$$

$$CD_\omega = 2(1 - F_1)\rho\sigma_{\omega 2}\frac{1}{\omega}\nabla k \cdot \nabla\omega$$

where $\nu_T = \mu_T/\rho$, $\sigma_{\omega 2}$ is a constant, F_1 is a flow state-dependent function, and σ_k, σ_ω, γ, β^* and β are weighted averages of corresponding constants of the standard $k-\omega$ and $k-\epsilon$ models with weights F_1 and $(1 - F_1)$, respectively [13].

COSA is second order accurate in time and space, and uses a very efficient MPI parallelization [14]. The accuracy of the space- and time-discretization has been thoroughly validated by considering a wide set of analytical and experimental test cases [5, 9, 12].

4. RESULTS

Thorough investigations into the 3D hydrodynamics of oscillating wings for power generation are reported herein. Most analyses are based on 3D time-accurate RANS simulations performed with COSA. The physical and computational set-up of all simulations is described first. Thereafter the 3D unsteady flow mechanisms accounting for the variations of the energy capture moving from the ideal scenario of an infinite wing to the realistic case of a finite wing are analyzed. Moreover, the dependence of the 3D flow patterns and, ultimately, of the energy capture efficiency on the wing end geometry is carefully examined.

4.1. physical and numerical set-up

The selected wing profile is the NACA0015 foil. The wing trajectory features a heaving and a pitching motion component defined by Eqs. (1) and (2) respectively. The operating condition characterized by a high efficiency of the energy extraction in the tur-

bulent flow regime described in [9] (case A) is considered. The heaving amplitude h_0 equals one chord and the pitching center is at $x_p = 1/3$ of the chord from the LE. The pitching amplitude θ_0 is 76.33^o and the nondimensionalized frequency $f^* = fc/u_\infty$ is 0.14, where f is the frequency in Hertz. The Reynolds number based on the freestream velocity and the foil chord is $Re = 1.5 \cdot 10^6$, and this value was used for all simulations reported below.

The time-dependent 3D turbulent flow fields past the oscillating wing were computed using structured multi-block non-deforming moving grids. In all simulations. the entire grid moved rigidly with the wing. The 3D grid was obtained by extruding the 2D grid past the foil along the spanwise direction. The node coordinates of 2D and 3D grids were nondimensionalized by the foil chord, and the farfield boundary in the foil plane was at about 50 chords from the foil. The required level of refinement of the 3D grid in the 2D plane of the foil was assessed by means of 2D simulations. More specifically, the periodic 2D flow field associated with the motion and flow parameters reported above was computed using a mesh with $98,304$ cells (coarse), one with $393,216$ cells (medium), and one with $1,575,864$ cells (fine) using 256 time-intervals per oscillation cycle. The overall mean power coefficients $\overline{C}_P$ obtained with the coarse and medium grids differed by 2.2%, whereas those obtained with the medium and fine grids differed by 0.4%, pointing to the suitability of the medium grid refinement for this problem. To assess the solution sensitivity to the level of temporal refinement, the selected regime was simulated with the 2D medium-refinement grid using 128, 256, 512 and 1024 time-intervals per oscillation period. The values of $\overline{C}_P$ obtained using 128 and 256 intervals differed by about 1.2%, whereas the difference between the 256-interval and the 512-interval $\overline{C}_P$, and the 512-interval and 1024-interval $\overline{C}_P$ were 0.7% and less than 0.1%, respectively. this highlighted that the solution was largely independent of the number of intervals per period when at least 512 time-intervals per period were used. In the light of this outcome and to keep the computational cost of the 3D analyses within the size of the available resources, the level of refinement of the 2D coarse grid was adopted for building the 2D sections of the 3D grid, and 256 time intervals per cycle were used in the 3D simulations analyzed below. It is the authors' view that the use of relatively coarse grids made herein does not significantly affect the main conclusions of the investigations presented below.

The 3D simulations used a symmetry boundary condition at midspan to halve computational costs. The $30,670,848$-cell grid was built by stacking a 2D $65,536$-cell O-grid in the spanwise direction from the midspan symmetry plane to the lateral farfield boundary which was at 50 chords from the symmetry boundary. The $65,536$-cell O-grid had 256 intervals along the foil, and 256 intervals in the normal-like
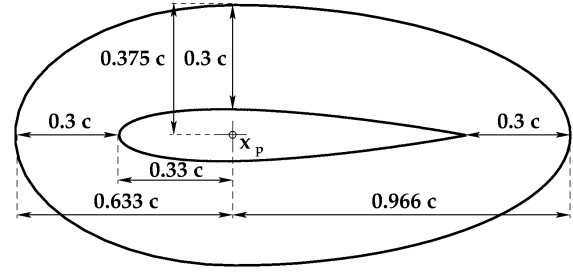

Figure 2. Endplate geometry.

direction. In the foil plane, the farfield boundary was at about 50 chords from the foil, and the distance d_w of the first grid points off the foil surface from the foil itself was about $6 \cdot 10^{-6}$. The AR of the wing was 10. Constant spanwise spacing $\Delta z = 0.02$ was used from midspan to 90 % semispan, and from here the grid was clustered towards the tip achieving a minimum spacing $\Delta z = 0.0003$. The cell size increased again moving from the tip to the lateral farfield boundary. Two wing end topologies were considered, one with sharp tips, the other with endplates. The geometry of the endplate is depicted in Fig. 2. Careful grid design enabled the use of the same grid for both configurations, removing any uncertainty in the comparative analysis of these two configurations arising from using different grid topologies. A view of two 3D grids is provided in Fig. 3.

The CFL number of the simulation of the wing with sharp tip and endplate were set to 4 and 3 respectively, and all simulations were run without multigrid. CFL ramping was used for all time steps, and 1,500 iterations were performed to compute the solution of each physical time. With this set-up, the residuals of the NS equations decreased by about 5 orders of magnitude at all physical times and all force and moment components fully converged within 1,000 to 1,100 iterations. All simulations were run until the maximum difference between C_Y over the last two oscillation cycles became less than 0.1% of the maximum C_Y over the last cycle. The number of oscillation cycles typically required to fulfil this requirement varied between four and ten, depending on the spatial and temporal refinement, and also on whether the simulation had been started from a freestream condition or from the solution of a simulation using the same grid but different temporal refinement. It was chosen to monitor the periodicity error of C_Y because the vertical force component gives the highest contribution to the extracted power. For all analyses of the oscillating wing presented in this report, y^+ was found to be smaller than one at all grid points and all times of the periodic flow field.

4.2. aerodynamic analysis

The evolution of the main kinematic parameters of the oscillating wing over one oscillation period is depicted in Fig. 4. The plot shows the time-dependent values of the vertical position h of the
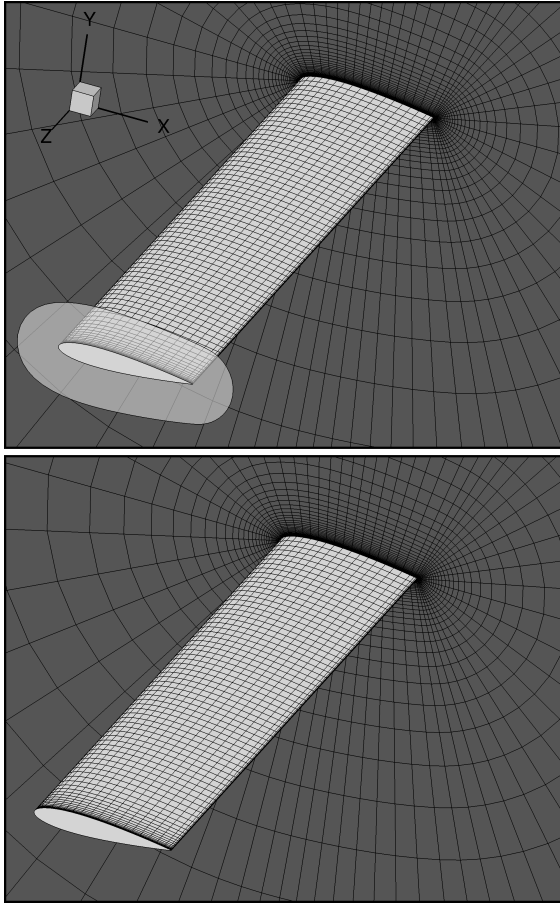
Figure 3. Surface mesh of wing and symmetry boundary (only every fourth grid line in all directions is reported). Top: wing with endplate. Bottom: wing with sharp tip.
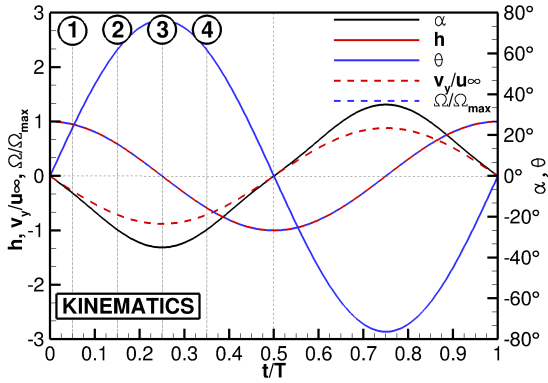
**Figure 4. Kinematic parameters.**

wing, its angular position θ, the nondimensionalized heaving velocity v_y/u_∞, and the nondimensionalized pitching velocity Ω/Ω_{max}, with Ω_{max} being the maximum pitching velocity of the cycle. The figure also reports the effective AoA α computed with Eq. (3). One notes that the maximum AoA is about 35°. The four positions labeled $1-4$ correspond to 5%,15%, 25% and 35% of the period respectively, and are

those at which the flow field is examined in greater detail in the following analyses.

Table 1. Mean power coefficients of wing with $AR \to \infty$, AR 10 and endplate (EP), and AR 10 and sharp tip (ST).

| AR	$\overline{C}_P$	$\overline{C}_{P_y}$	$\overline{C}_{P_\theta}$
∞	1.004	1.176	-0.172
10 EP	0.941	1.219	-0.278
10 ST	0.882	1.149	-0.267

The mean values of the overall power coefficient $\overline{C}_P$, the heaving power coefficient $\overline{C}_{P_y}$, and the pitching power coefficient $\overline{C}_{P_\theta}$ for the infinite span wing, the AR 10 wing with endplate (EP) and the AR 10 wing with sharp tip (ST) are reported in Table 1. The infinite span analysis was performed with a 2D simulation, whereas the two AR 10 analyses are based on full 3D simulations. One notes that $\overline{C}_P$ of the AR 10 wing with EPs is 6% lower than that of the infinite wing, whereas $\overline{C}_P$ of the AR 10 wing with STs is 12% lower than that of the ideal infinite wing case. The breakdown of the heaving and pitching power components for the three cases highlights that: *a)* the mean negative pitching power (a loss term) of both AR 10 wings increases by a comparable amount with respect to the ideal infinite span case (36% with STs and 38% with EPs), *b)* the heaving power coefficient of the AR 10 wing with STs also decreases (by about 2%) with respect to the ideal case, whereas the heaving power coefficient of the AR 10 wing with EPs increases by about 4%. These observations highlight that 3D flow effects hit the overall energy extraction efficiency of this device in a complex manner, that appears to depend on the geometry of the wing tips.
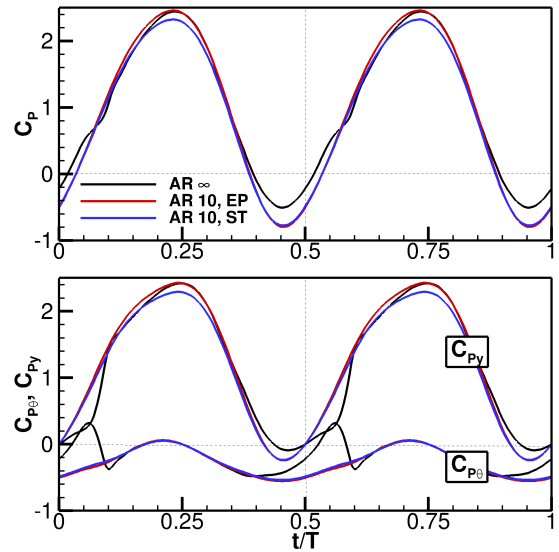
**Figure 5. Comparison of overall, heaving and pitching power coefficients.**

The two subplots of Fig. 5 report the profiles of C_P, C_{P_y} and C_{P_θ} over the period. In the first 10% and last 15% of both semi-periods, both AR 10 C_P profiles are significantly lower than the $AR\,\infty$ configuration (top subplot). This is due to the higher negative pitching power of both finite wings when the wing is at the highest and lowest points of the stroke (bottom subplot). Fig. 5 also highlights that, between about 10% and 35% of both semi-periods, the heaving and overall power coefficients of the wing with EPs are higher than for the ideal wing, whereas those of the wing with STs are lower.
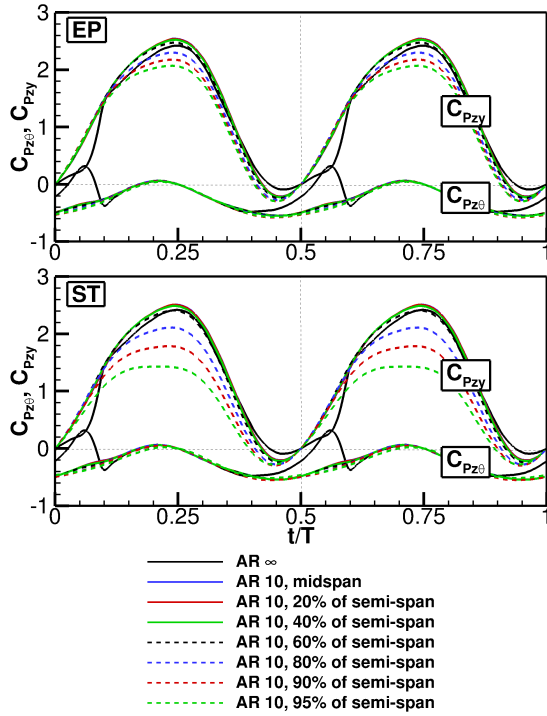
Figure 6. Comparison of heaving and pitching power coefficients per wing length.

To further investigate the dependence of the energy extraction efficiency of the finite span wing on the tip geometry highlighted in Fig. 5, the power coefficient curves per unit length of the AR 10 wings at various spanwise positions are cross compared in Fig. 6, which also reports the $AR\,\infty$ profiles for reference. The symbols $C_{P_{zy}}$ and $C_{P_{z\theta}}$ denote respectively the heaving and pitching power coefficients per wing length. One notes that between about 10% and 35% of both semi-periods the reduction of $C_{P_{zy}}$ with respect to the ideal case as one moves from about 80% semispan towards the tip is significantly smaller for the wing with EPs than for the wing with STs. Moreover, in the same portions of the period, the heaving power of the finite span wing is higher with EPs than with STs. These performance differences are due primarily to the existence of a strong tip vortex in the ST configuration, which induces significant downwash lowering the effective AoA with a strength decreasing from tip to midspan. Note

also that the largest differences between the heaving power of the two AR 10 wings occur in the period range with maximum nominal AoA. The comparison of the skin friction lines of the two finite span wings at 25 % of the vertical stroke are reported in Fig. 7, which highlights the distortions of the flow path of the wing with STs leading to the formation of the tip vortex. The $C_{P_{z\theta}}$ profiles of Fig. 6 also show that the
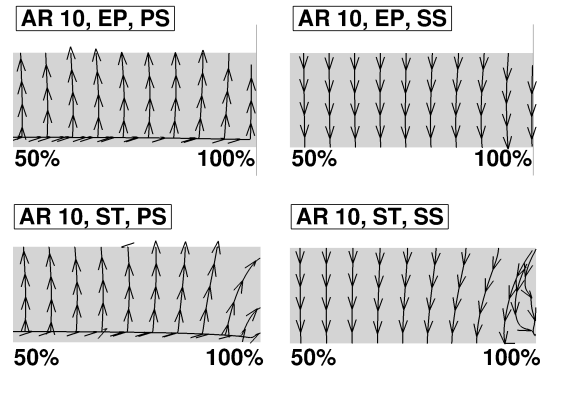
Figure 7. Skin friction lines on pressure side (PS) and suction side (SS) of wing with sharp tips and endplates at 25% **of the cycle.**

maximum loss-generating increment of the negative pitching power occurs when the finite span wings is close to the highest and lowest positions of the vertical stroke, varies fairly little along the span, and is not significantly affected by the wing tip geometry. As highlighted below, this is due to the absence of LEVS in the 3D flow field of both AR 10 wings.

The two top subplots of Fig. 8 depict the contours of the z-component of the vorticity of the infinite span wing and the midspan section of the AR 10 wing with EPs at 5% of the period (position 1). The botom subplots refer instead to the 25% point of the period (position 3). The comparison of the top subplots highlights that in the AR 10 configuration, unlike in the infinite span case, there is no LEVS. The low pressure region on the foil side on which the vortex is generated contributes to reduce the energy capture loss due to the negative pitching power. Therefore, the absence of LEVS in the AR 10 case results in higher losses due to the larger (in absolute value) negative pitching power. In the other portions of the period, where LEVS is absent also in the infinite span case, the flow at midspan of the AR 10 wing and that of the wing with no tip effects are nearly identical, as highlighted by the bottom subplots which refer to the position of maximum nominal AoA. These observations also hold for the midspan section of the AR 10 wing with STs, the vorticity contours of which are not reported for brevity. The observations confirm that this loss mechanism arising when dealing with finite span wings is fairly independent of the tip geometry.
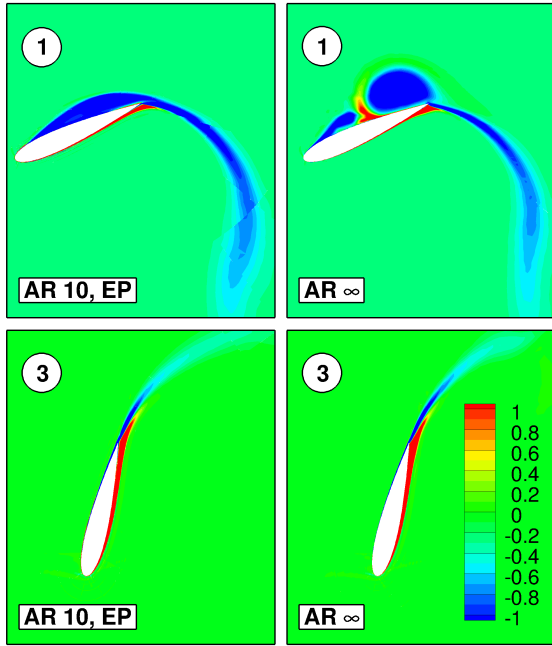
Figure 8. Contours of z component of vorticity of wing with infinite span and at midspan of wing with EPs. Top left: wing with EPs at 5 % of the cycle; top right: infinite wing at 5 % of the cycle; bottom left: wing with EPs at 25 % of the cycle; bottom right: infinite wing at 25 % of the cycle.
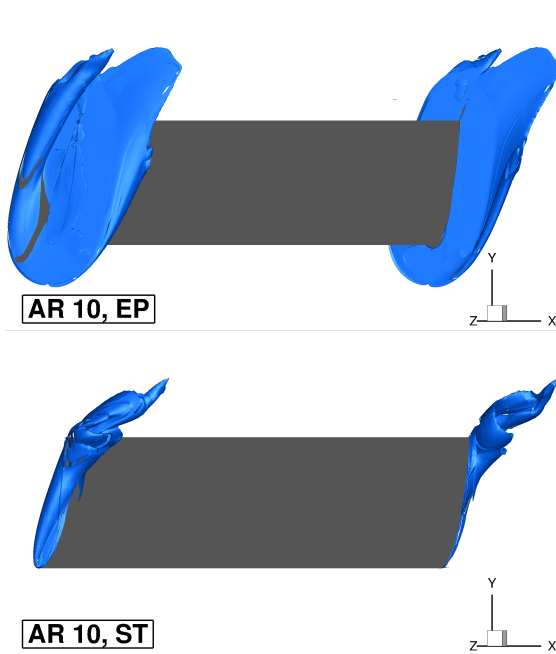

Figure 9. Isosurface of vorticity magnitude ($\Omega_m = 2$) at 25 % of the period. Top: wing with endplates. Bottom: wing with sharp tips.

The top and bottom subplots of Fig. 9 show the isosurface of vorticity magnitude ($\Omega_m = 2$) at the tips of the wings with endplates and sharp tips respect-

ively. At the sharp tips vorticity from the pressure side rolls down to the suction side to form a trailing vortex, which causes the downwash effect. The downwash leads to a reduction of the effective AoA to the sections close to the tip, reducing C_{P_y}, as observed in the bottom plot of Fig. 6. The top plot of Fig. 9 shows that a tip vortex exists also for the wing with endplates. This vortex, however, originates at the edge of the endplates and is farther away from the wing than the vortex of the wing with sharp tips, resulting in less pronounced downwash. Moreover the vortex originating at the endplate is smaller than that originating at the sharp tip, because the driving pressure difference is smaller in the former case.
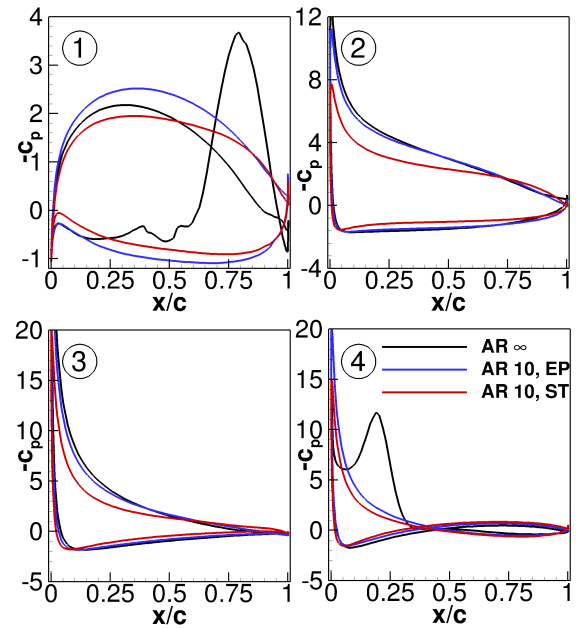

Figure 10. Pressure coefficient c_p of infinite span wing, and AR 10 wings with endplates and sharp tips at positions labeled 1-4 in Fig. 4.

The effects of the flow mechanisms discussed above on the static pressure distribution of the wing, which is a measure of the loading, are examined in Fig. 10. Its four subplots compare the static pressure coefficient of the infinite wing, and the 95 % semispan section of the AR 10 wings at the positions labeled 1-4 in Fig. 4. All four subplots show that the pressure-based heaving force acting on the wing with endplates is always larger than that on the wing with sharp tips, and this is due to the stronger downwash of the wing with sharp tips, which reduces the effective AoA. At positions 2 and 3, close to maximum nominal AoA, the heaving force per unit length of the infinite span wing is comparable to that of the wing with endplates. At position 1, corresponding to the LE vortex of the infinite wing being close to the trailing edge, the heaving force of the infinite wing is significantly smaller than that of the finite span wings.

5. SUMMARY

A detailed numerical investigation into the impact of flow three-dimensionality on the energy extraction efficiency of oscillating finite span wings were performed. Using the COSA 3D NS code with 30 million-cell grids, the differences of flow patterns and performance parameters between an infinite wing and one with aspect ratio 10 with either sharp tips or endplates were investigated.

The considered wing motion is characterized by a high power generation efficiency of the infinite wing in a turbulent regime at $Re = 1.5 \cdot 10^6$, and this operating condition is characterized by the existence of LEVS. The mean overall power coefficient of the AR 10 wing with sharp tips is found to decrease by 12 % with respect to that of the infinite wing. The loss is caused both by the reduction of the effective AoA induced by the downwash associated with the strong tip vortices, and also the LEVS suppression, which yields higher pitching power in the infinite span case. The mean overall power coefficient of the AR 10 wing with endplates is found to decrease by only 6 % with respect to the infinite wing. The lower loss with respect to the wing with sharp tips is due to a smaller reduction of the effective AoA due in turn to a weaker downwash achieved by weakening the tip vortices with the endplates.

For the AR 10 wing, the reduction of energy capture efficiency due to the LEVS suppression is independent of the tip geometry. A recent optimization study aiming at determining combinations of kinematic parameters (oscillation frequency, heaving and pitching amplitudes) to maximize the energy capture efficiency highlighted that high efficiency levels can be achieved also with kinematic conditions which do not yield LEVS [10]. In the light of the loss associated with the suppression of LEVS when considering finite wing effects, it appears advisable to design these devices avoiding regimes characterized by 2D LEVS, so as to minimize losses due to finite wing effects.

ACKNOWLEDGEMENTS

REFERENCES

[1] McKinney, W., and DeLaurier, J., 1981, "The Wingmill: An Oscillating-Wing Windmill", *Journal of Energy*, Vol. 5 (1), pp. 109–115.

[2] Jones, K., Lindsey, K., and Platzer, M., 2003, "An Investigation of the Fluid-Structure Interaction in an Oscillating-Wing Micro-Hydropower Generator", Chakrabarti, Brebbia, Almozza, and Gonzalez-Palma (eds.), *Fluid Structure Interaction 2*, WIT Press, Southampton, United Kingdom, pp. 73–82.

[3] Young, J., Lai, J., and Platzer, M., 2014, "A review of progress and challenges in flapping foil power generation", *Progress in Aerospace Sciences*, Vol. 67, pp. 2–28.

[4] Kinsey, T., and Dumas, G., 2008, "Parametric Study of an Oscillating Airfoil in a Power-Extraction Regime", *AIAA Journal*, Vol. 46 (6), pp. 1318–1330.

[5] Campobasso, M., and Drofelnik, J., 2012, "Compressible Navier-Stokes analysis of an oscillating wing in a power-extraction regime using efficient low-speed preconditioning", *Computers and Fluids*, Vol. 67, pp. 26–40.

[6] Kinsey, T., Dumas, G., Lalande, G., Ruel, J., Mehut, A., Viarogue, P., Lemay, J., , and Jean, Y., 2011, "Prototype testing of a hydrokinetic turbine based on oscillating hydrofoils", *Renwable energy*, Vol. 36, pp. 1710–1718.

[7] Kinsey, T., and Dumas, G., 2012, "Computational Fluid Dynamics Analysis of a Hydrokinetic Turbine Based on Oscillating Hydrofoils", *Journal of Fluids Engineering*, Vol. 134, pp. 021104.1–021104.16.

[8] Spalart, P., and Allmaras, S., 1994, "A one-equation turbulence model for aerodynamic flows", *La Recherche Aerospatiale*, Vol. 1, pp. 5–21.

[9] Campobasso, M., Piskopakis, A., Drofelnik, J., and Jackson, A., 2013, "Turbulent Navier-Stokes Analysis of an Oscillating Wing in a Power-Extraction Regime Using the Shear Stress Transport Turbulence Model", *Computers and Fluids*, Vol. 88, pp. 136–155.

[10] Kinsey, T., and Dumas, G., 2014, "Optimal Operating Parameters for an Oscillating Foil Turbine at Reynolds Number 500,000", *AIAA Journal*, Vol. 52 (9), pp. 1885–1895.

[11] Kinsey, T., and Dumas, G., 2012, "Three-Dimensional Effects on an Oscillating-Foil Hydrokinetic Turbine", *Journal of Fluids Engineering*, Vol. 134, pp. 071105.1–071105.11.

[12] Campobasso, M., Gigante, F., and Drofelnik, J., 2014, "Turbulent Unsteady Flow Analysis of Horizontal Axis Wind Turbine Airfoil Aerodynamics Based on the Harmonic Balance Reynolds-Averaged Navier-Stokes Equations", ASME paper GT2014-25559.

[13] Menter, F., 1994, "Two-Equation Turbulence-Models for Engineering Applications", *AIAA Journal*, Vol. 32 (8), pp. 1598–1605.

[14] Jackson, A., and Campobasso, M., 2011, "Shared-memory, Distributed-memory and Mixed-mode Parallelization of a CFD Simulation Code", *Computer Science Research and Development*, Vol. 26 (3-4), pp. 187–195.